



# The dominant role of the atmospheric component of coupled models in ENSO amplitude simulations

Yanli Tang<sup>1</sup> · Lijuan Li<sup>1</sup> · Bin Wang<sup>1,2</sup> · Pengfei Lin<sup>1</sup> · Lin Chen<sup>3</sup> · Feng Xie<sup>1</sup> · Wenjie Dong<sup>4</sup> · Kun Xia<sup>1</sup>

Received: 18 February 2018 / Accepted: 21 August 2018 / Published online: 28 August 2018  
© Springer-Verlag GmbH Germany, part of Springer Nature 2018

## Abstract

To explore the relative contributions of the atmospheric and oceanic components of coupled models to ENSO amplitude simulations, we innovatively “assembled” four coupled models and performed analyses on their ENSO simulations. Specifically, the atmospheric and oceanic components of two commonly used coupled models are cross-coupled to construct four parent models. Based on the simulated ENSO amplitude, the four parent models are classified into two groups: Grid-point Atmospheric Model of IAP LASG Version 2 (GAMIL2)-based models whose ENSO amplitudes are comparable to (although slightly weaker than) observations, and Community Atmosphere Model Version 4.0 (CAM4)-based models whose ENSO amplitudes reach up to twice those of observations. The BJ-index analysis reveals that the atmospheric components modulate ENSO amplitude by affecting the atmospheric thermodynamic (TD) feedback and the oceanic thermocline (TH) feedback. The TD feedback biases in the CAM4-based models are attributable to an overly negative low-cloud fraction feedback and low-cloud liquid water feedback in the Niño-3 region. The underestimated TH feedback in the GAMIL2-based models is due to an underestimated mean upwelling ( $\bar{w}$ ), while the seemingly accurate TH term in the CAM4-based models is the result of compensation by an overestimated regression of zonal tilt of the thermocline on the equatorial zonal wind stress ( $\beta_h$ ) and an underestimated  $\bar{w}$ . Furthermore,  $\beta_h$  dominates TH differences in the two atmospheric groups, and is mainly associated with the normalized wind stress anomaly over the Niño-4 region and the vertical ocean subsurface temperature structure.

**Keywords** GAMIL2-based models · CAM4-based models · BJ-index · Thermodynamic feedback · Thermocline feedback

## 1 Introduction

The El Niño–Southern Oscillation (ENSO), originating from tropical ocean–atmosphere interactions, is the most prominent inter-annual climate variation in the tropical Pacific

(McPhaden et al. 2006). The El Niño, warm phase of the ENSO, is characterized by large-scale warming in the eastern tropical Pacific, and a series of corresponding climatological anomalies in the tropical Pacific. For example, convection associated with the Walker Circulation moves into the central Pacific from the western Pacific and weakened trade winds promote warmer water in the western Pacific to surge eastward, leading to a flattening of the tropical eastern–western thermocline contrast and a reduction in upwelling in the eastern Pacific (Christensen et al. 2013). Correspondingly, the La Niña, cold phase of the ENSO, generally has conditions inverse to those of El Niño. These fluctuations of the ENSO will bring about significant anomalies in weather, agriculture, and disease in many parts of the world (Donnelly and Woodruff 2007; Callaghan and Power 2011; Hammer et al. 2001; Kovats et al. 2003). Although Coupled Model Intercomparison Project Phase 5 (CMIP5) models in historical simulations show some improvements in ENSO amplitude compared to CMIP3 (Bellenger et al. 2014), El Niño intensity in future emission scenarios

✉ Lijuan Li  
ljli@mail.iap.ac.cn

<sup>1</sup> State Key Laboratory of Numerical Modeling for Atmospheric Sciences and Geophysical Fluid Dynamics (LASG), Institute of Atmospheric Physics, Chinese Academy of Sciences, Beijing 100029, China

<sup>2</sup> Ministry of Education Key Laboratory for Earth System Modeling, Center of Earth System Science (CESS), Tsinghua University, Beijing, China

<sup>3</sup> International Pacific Research Center, and School of Ocean and Earth Science and Technology, University of Hawai‘i at Mānoa, 2525 Correa Rd., Honolulu, HI 96822, USA

<sup>4</sup> School of Atmospheric Sciences, Sun Yat-sen University, Zhuhai, China

remains largely uncertain (Guilyardi et al. 2012; Stevenson et al. 2012; Chen et al. 2015a, b, 2017). The large uncertainty in ENSO intensity may be primarily associated with differences in the internal feedbacks among the models (Kim et al. 2014). Therefore, process-oriented ENSO metrics have been widely used in evaluating ENSO simulations and providing a perspective on the feedback processes that induce ENSO biases in climate models (Bellenger et al. 2014; An et al. 2017).

The ENSO is a complex phenomenon and can be affected by many processes. Many studies of oceanic processes (e.g., Jin 1997; Kim and Jin 2011b; An et al. 2017) have emphasized the importance of the thermocline feedback, i.e., the vertical advection of anomalous subsurface temperature by mean upwelling. Other studies investigated the zonal advection feedback that stems from the zonal advection of mean SST by anomalous currents and found that it tends to work constructively with the thermocline feedback through a geostrophic balance, and also contributes to the growth and phase transition of the ENSO (An and Jin 2001). The role of atmospheric feedbacks has recently received increased attention (Sun et al. 2006; Guilyardi et al. 2004; Dommenges et al. 2010; Rädcl et al. 2016; Lloyd et al. 2012; Chen et al. 2013). In particular, the positive wind-SST feedback [measured as the regression coefficient between zonal wind stress in the Niño-4 region (5°N–5°S, 160°E–210°E) and SST anomalies averaged over the Niño-3 region (5°N–5°S, 150°–90°W)] and the negative heat flux-SST feedback [measured as the regression coefficient between net heat flux at the surface and SST anomalies in the Niño-3 region], collectively influence the overall performance of ENSO simulations (Guilyardi et al. 2004; Lloyd et al. 2012). Additionally, overall ENSO dynamics can be described by the Bjerknes stability index (BJ index; Jin et al. 2006), which indicates the growth rate of SST anomalies and is a useful tool for measuring the stability strength of the coupled ENSO mode. Furthermore, it includes atmospheric and oceanic feedbacks associated with ENSO variability and has been adopted to explore ENSO dynamics in several recent climate studies (Lübbecke and McPhaden 2013; Kim et al. 2014; Chen et al. 2016).

Generally, simulations of oceanic and atmospheric feedbacks are still underestimated or overestimated (Bellenger et al. 2014; Kim et al. 2014), which may lead to biases in ENSO variability, or seemingly accurate ENSO amplitudes that are based on incorrect physical mechanisms. The factors causing ENSO amplitude biases and their related feedbacks are complex, and may be associated with the convective parameterization scheme, nonconvective condensation processes in atmospheric processes (Neale et al. 2008; Li et al. 2014), or the vertical mixing parameterization, background vertical diffusivity in oceanic processes (Meehl et al. 2001; Sun et al. 2009; Guilyardi 2006; An and Choi 2013). For instance, Tang et al. (2016) traced the source of ENSO

simulation differences to the atmospheric component of two CGCMs, while Meehl et al. (2001) identified a more important role for the oceanic component in two coupled models. However, the relative contributions of the atmospheric and oceanic model components of current coupled models to ENSO strength biases and its related feedbacks are difficult to distinguish as most coupled models have different atmospheric and oceanic models. To clearly identify their respective contributions, the CESM1.2.0 (known to simulate a strong ENSO amplitude) and the Flexible Global Ocean–Atmosphere–Land System Model (Grid-point Version 2; FGOALS-g2; known to simulate an amplitude close to observations; Kim et al. 2014; Bellenger et al. 2014) are selected, and their two atmospheric and oceanic components are cross-coupled to construct four parent models: CESM-g2, FGOALS-g2, CESM and FGOALS-c4. A BJ-index analysis is used to characterize the ENSO differences among the above four parent models, and the relative roles of the atmospheric and oceanic components in determining ENSO amplitude are determined using the contributing terms of the BJ-index.

The remainder of the paper is organized as follows: in Sect. 2, the four parent models (FGOALS-g2, CESM-g2, CESM and FGOALS-c4), observational and reanalysis datasets, and the BJ-index used in this study are described. The different ENSO amplitudes of the four parent models are described in Sect. 3. The BJ-index features and the most important feedbacks associated with ENSO variability are presented, and the dominant model component is identified by the most contributing feedbacks of the BJ-index in Sect. 4. The results are summarized and discussed in Sect. 5.

## 2 Model, data and analytical methods

### 2.1 Four parent models

The CESM1.2.0 (hereafter referred to as CESM) was developed by the National Centre for Atmospheric Research (NCAR). The atmospheric component of the CESM we select is the Community Atmosphere Model Version 4.0 (CAM4; Neale et al. 2013), which adopts a hybrid pressure sigma coordinate with 30 layers in the vertical and a finite-volume grid with a resolution of 2° in horizontal. The oceanic component of the CESM is the Parallel Ocean Program Version 2 (POP2; Smith et al. 2010) with a 1° displaced pole grid. The land surface model and the ice model are the Community Land Surface Model Version 4.0 (CLM4; Oleson et al. 2010) and the Los Alamos Sea Ice Model Version 4 (CICE4; Hunke and Lipscomb 2008).

The other existing parent model used here is the FGOALS-g2, developed by the LASG, IAP, Chinese Academy of Sciences, and its atmospheric component is

the Grid-point Atmospheric Model of IAP LASG Version 2 (GAMIL2). The GAMIL2 uses a dynamical core that includes a finite difference scheme and a two-step shape-preserving advection scheme, and adopts a sigma coordinate with 26 layers in the vertical and a hybrid horizontal grid (2.8° Gaussian grid and a weighted equal-area grid) in the horizontal (Wang et al. 2004; Li et al. 2013b). The oceanic component of FGOALS-g2 is the LASG IAP Climate System Ocean Model version 2 (LICOM2; Liu et al. 2012), which uses a latitude–longitude grid with a horizontal resolution of 1° (0.5° meridional refined resolution in the tropics) and an adjusted vertical resolution in the upper layers (10 m for each layer in the upper 150 m; Wu et al. 2005). The land and ice model of FGOALS-g2 are the CLM3 and CICE4-LASG, respectively (Li et al. 2013a).

The CESM-g2 is constructed by nesting the GAMIL2 into the CESM, mentioned above (Tang et al. 2016), and the FGOALS-c4 is constructed by nesting the CAM4 into the FGOALS-g2. In other words, the two atmospheric components (CAM4 and GAMIL2) and the two oceanic components (POP2 and LICOM2) are cross coupled to create the four parent models, and their relationships are shown in Fig. 1. The CESM and FGOALS-c4 have the same atmospheric component (CAM4), and both the FGOALS-g2 and CESM-g2 have the same atmospheric component (GAMIL2), while the CESM and CESM-g2 share the same oceanic component (POP2), and the FGOALS-g2 and FGOALS-c4 share the same oceanic component (LICOM2).

In order to isolate internal variability, we perform pre-industrial (PI) experiments and integrate over 500 years using the CESM, CESM-g2 and FGOALS-c4 models. The PI-control simulation (years 101–500) of FGOALS-g2 are obtained from CMIP5 for comparison. We quantify ENSO amplitude using the standard deviations of area-averaged monthly SST anomalies (SSTA) over the Niño-3 (5°N–5°S, 150°–90°W), Niño-4 (5°N–5°S, 160°E–150°W) and Niño-3.4 (5°N–5°S, 190°E–240°E) regions. The anomalies are calculated by

subtracting the seasonal cycle from individual model results or observation climatologies.

### 2.2 Validation datasets and BJ index

The validation datasets used in this study are as follows: the SST is from the merged products of HADISST1 [Met. Office Hadley Centre sea ice and SST dataset (1870 onward) and National Oceanic and Atmospheric Administration Optimum Interpolation SST Version 2 dataset (November 1981 onward; Hurrell et al. 2008)]; the vertical velocities at 500 hPa, heat fluxes and surface wind stress data for the period 1958–2001 are supplied by the ERA-40 (40-year European Centre for Medium-Range Weather Forecasts Re-Analysis; Uppala et al. 2005); The Liquid Water Path and cloud cover during years 1984–2009 are obtained from the ISCCP (International Satellite Cloud Climatology Project; Rossow and Schiffer 1999). The Simple Ocean Data Assimilation Reanalysis version 2.2.4 (SODA2.2.4; Carton and Giese 2008; Giese and Ray 2011) is used for three-dimensional ocean temperature and velocity.

The BJ-index adopted in this paper follows that of Jin et al. (2006) with the modifications of Kim and Jin (2011a), and is formulated as follows:

$$BJ = \frac{R - \epsilon}{2} \quad \text{and} \quad (1)$$

$$R = -(a_1 \frac{\langle \Delta \bar{u} \rangle_E}{L_x} + a_2 \frac{\langle \Delta \bar{v} \rangle_E}{L_y}) - \alpha_s + \mu_a \beta_u \left\langle -\frac{\partial \bar{T}}{\partial x} \right\rangle_E + \mu_a \beta_w \left\langle -\frac{\partial \bar{T}}{\partial z} \right\rangle_E + \mu_a \beta_h \left\langle -\frac{H(\bar{w})\bar{w}}{H_1} \right\rangle_E \quad (2)$$

where  $\epsilon$  is a damping rate related to the ocean adjustment as obtained through multiple regression using Eq. (10) in Kim and Jin (2010),  $u$ ,  $v$  and  $w$  are the ocean zonal, meridional and vertical velocities, respectively, in the mixed layer,  $T$  denotes SST,  $\langle \cdot \rangle_E$  represents a volume average over the eastern box (180°E–80°W, 5°S–5°N) throughout the mixed-layer,  $L_x$  and  $L_y$  are the zonal and meridional extent of the averaging box,  $a_1$  and  $a_2$  are calculated by linear regression using SST anomalies zonally or meridionally averaged at the boundaries of an area averaging box and SST anomalies averaged over the box,  $H(x)$  is a step function to ensure that only the upward vertical motion affects surface temperature and  $H_1$  is the mixed-layer depth set at a constant value of 50 m in this analysis. The overbars denote the climatological mean. The term  $R$ , which collectively represents the ENSO-relevant feedback processes of tropical atmosphere–ocean interactions, consists of two negative feedbacks and three positive feedbacks: the first two terms represent dynamic damping by mean advection (MA;  $a_1 \frac{\langle \Delta \bar{u} \rangle_E}{L_x} + a_2 \frac{\langle \Delta \bar{v} \rangle_E}{L_y}$ ) and

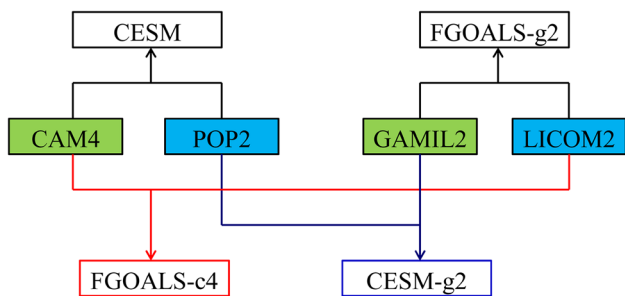


**Fig. 1** Relationship diagram for the four parent models: CESM, FGOALS-g2, FGOALS-c4 and CESM-g2. The green-filled and blue-filled textboxes denote the atmospheric and oceanic components, respectively

thermodynamic damping (TD;  $\alpha_s$ ), that make negative contributions; the last three terms represent positive feedbacks that act to enhance the SST anomaly and thus make positive contributions to the BJ index, including zonal advective (ZA;  $\mu_a \beta_u \langle -\frac{\partial \bar{T}}{\partial x} \rangle_E$ ), Ekman (EK;  $\mu_a \beta_w \langle -\frac{\partial \bar{T}}{\partial x} \rangle_E$ ), and thermocline (TH;  $\mu_a \beta_h \langle \frac{H(\bar{w})\bar{w}}{H_1} \rangle_E a_h$ ) feedbacks. The three positive feedbacks all contain the parameter  $\mu_a$  (a basin wide zonal wind stress response to an SST anomaly in the eastern equatorial basin). The terms  $\beta_u$ ,  $\beta_w$  and  $\beta_h$  represent the response of oceanic factors (ocean zonal currents, upwelling and thermocline depth, respectively) to the wind stress. The term  $a_h$  denotes the response of the ocean subsurface temperature to thermocline depth. A detailed derivation for the BJ-index is shown in Kim and Jin (2011a, b).

### 3 ENSO amplitudes in the four parent models

After a 100-year spin up in the PI-control runs, the linear trends of global mean SST in CESM-g2, FGOALS-g2, CESM and FGOALS-c4 are  $2.53 \times 10^{-4}$  K year<sup>-1</sup>,  $1.84 \times 10^{-4}$  K year<sup>-1</sup>,  $2.52 \times 10^{-4}$  K year<sup>-1</sup> and  $1.67 \times 10^{-4}$  K year<sup>-1</sup>, respectively. All four models have a small climate drift and tend to be stable. The standard deviation of the area-averaged monthly SST anomalies (SSTA) of the four parent models over the Niño-3 region (5°N–5°S, 150°–90°W) during years 401–500 are provided in Table 1. The four models are separated into two groups by comparing the simulated ENSO amplitudes with those of observations: the CESM and FGOALS-c4 with overestimated ENSO amplitude fall into the ‘strong ENSO amplitude’ group, while the CESM-g2 and FGOALS-g2 with underestimated ENSO amplitude fall into the ‘weak ENSO amplitude’ group. Note that the ENSO amplitude in FGOALS-g2 is close to observations, although FGOALS-g2 falls into the second group. Moreover, the same phenomenon (the division between strong and weak response groups) occurs when either the Niño-4 (5°N–5°S, 160°E–150°W) or the Niño-3.4

**Table 1** Standard deviations of the area-averaged monthly SST anomalies (SSTA) over the Niño-3 (5°N–5°S, 150°–90°W), Niño-4 (5°N–5°S, 160°E–150°W) and Niño-3.4 (5°N–5°S, 190°E–240°E) regions for HadISST observations during 1901–2000, and the four parent models (CESM-g2, FGOALS-g2, CESM and FGOALS-c4) during years 401–500 from the PI-control run

	HadISST	CESM-g2	FGOALS-g2	CESM	FGOALS-c4
Niño-3	0.81	0.63	0.77	1.37	1.37
Niño-3.4	0.77	0.52	0.77	1.32	1.49
Niño-4	0.55	0.39	0.51	1.03	1.36

(5°N–5°S, 190°E–240°E) regions are used in the analysis. In addition, the above results hold when any other 100-year time slice during years 101–500 is used for the comparison (not shown). For simplicity, the difference of ENSO amplitude during the last 100 years (i.e., year 401–500) is the focus of the following analysis. Interestingly, we note that the two coupled models (CESM and FGOALS-c4) in the strong ENSO amplitude group share the same atmospheric component (CAM4) and the CESM-g2 and FGOALS-g2 in the weak ENSO amplitude group also share the same atmospheric component (GAMIL2). Although the CESM (FGOALS-c4) has the same components as the CESM-g2 (FGOALS-g2) except for the atmospheric model, the ENSO amplitude in the former is twice as large as that in the latter, indicating the dominant role of the atmospheric component of the coupled models in ENSO amplitude simulations. However, although the high and weak ENSO strength groups share the same atmospheric models, the ENSO amplitudes in each group still differ to some extent as indicated in Table 1, implying the oceanic component also plays a role in ENSO amplitude simulations; however, the contribution of the oceanic component is noticeably smaller than that of the atmospheric component in the four parent models.

To reveal the ENSO temporal and spatial characteristics among the four model simulations, a time series of the Niño-3 index and spatial distributions of SSTA STD in the tropical Pacific from HadISST observations and the four PI-control runs are compared in Fig. 2. The CAM4-based models (CESM and FGOALS-c4) result in continuously strong SSTA variations, whereas the GAMIL2-related models (CESM-g2 and FGOALS-g2) simulate relatively weak variability (Fig. 2a–e). The FGOALS-g2 results exhibit a statistical variability close to observations, consistent with the SSTA STD averaged over the Niño-3 region. Moreover, the CAM4-based models (Fig. 2i, j) have greatly enhanced SSTA variability compared with the GAMIL2-based models (Fig. 2g, h) over the whole tropical Pacific. The large SSTA STD values in the weak ENSO group are confined to the tropical eastern Pacific, whereas those in the strong ENSO group extend westward and poleward. In addition to the ENSO amplitude, other ENSO characteristics, such as the power spectrum and phase lock, in the four simulations may be closely associated with their atmospheric models (Figure not shown). However, this study focuses on ENSO amplitude, specifically why CGCMs with different atmospheric components show marked differences in representing ENSO amplitude, and what physical mechanisms are involved.

### 4 Factors contributing to ENSO amplitude differences

To investigate the causes of the differing ENSO amplitudes simulated by the four parent models, we carry out a diagnosis based on the BJ-index. Figure 3 shows the values of the

BJ-index and its contributing terms from SODA data and the four parent models. In the GAMIL2-based models, the magnitude of the BJ-index in FGOALS-g2 is close to, although slightly less than, the reanalysis SODA data. The CESM-g2 values have a more negative bias, which causes the underestimation in ENSO amplitude. In contrast, the BJ-index in the CAM4-based models (CESM and FGOALS-g4) are both overestimated in the opposite direction, leading to an overestimation of ENSO amplitude. Our diagnosed results show that the biases in BJ-index agree well with the biases in ENSO amplitude simulations. Among the five contributing terms, there are two factors that have noticeable variability and play the dominant roles in BJ-index variability. These are the thermodynamic (TD) feedback and the thermocline (TH) feedback. As pointed out in previous studies (Lloyd et al. 2012; Kim and Jin 2011b), the TD term is related to the atmospheric feedback and TH is one of the oceanic feedbacks. We next explore how the different model components affect the BJ-related terms, particularly the TD and TH terms.

#### 4.1 Differences in thermodynamic (TD) feedbacks

As shown in Fig. 3, TD feedbacks in the GAMIL2-based coupled models (CESM-g2 and FGOALS-g2) are much closer to the SODA-ERA40 data, while those of the CAM-related models (CESM and FGOALS-c4) are much weaker, particularly for the FGOALS-c4. The weak TD feedbacks cannot prevent the sustainable development of ENSO effectively in the CESM and FGOALS-c4 models, leading to a strong ENSO amplitude. This highlights the influence of the atmospheric component on simulations of the atmospheric heat-flux feedback. As one of the primary contributors to the BJ-index, the TD feedback is calculated from the net heat-flux feedback. Because the net heat-flux (QNET) is equal to the net shortwave radiation (SW) minus the sum of the net longwave radiation (LW) and the sensible (SH) and latent heat fluxes (LH), the QNET feedback is split into four components: SW, LW, SH and LH feedbacks. The component feedback is calculated as the regression coefficient between the individual flux at the surface and SST anomalies in the Niño-3 region. As shown in Fig. 4, among the four models, the differences in the LW and SH feedbacks are relatively small—the LH feedbacks have a difference of  $3.372 \text{ W m}^{-2}$  at most, while the SW feedbacks have a difference of  $14.82 \text{ W m}^{-2}$  and dominate the net heat-flux feedback differences. The Niño-3 averaged value of the SW feedback from ERA40 is  $-11.49 \text{ W m}^{-2} \text{ K}^{-1}$ . The SW feedbacks simulated by the CESM-g2 and FGOALS-g2 are  $-11.24$  and  $-8.57 \text{ W m}^{-2} \text{ K}^{-1}$ , respectively, and are of comparable strength to that of ERA40. In contrast, the SW feedbacks are underestimated in CESM and FGOALS-c4 ( $-2.25$  and  $3.58 \text{ W}$

$\text{m}^{-2} \text{ K}^{-1}$ , respectively). Figure 5 shows the spatial distribution of SW feedbacks for observations and the four parent models. The GAMIL2-based coupled models (Fig. 5b, c) exhibit a similar negative distribution of SW feedbacks in most tropical Pacific regions (although the feedback is a little weaker for FGOALS-g2), while the CAM4-based coupled models (Fig. 5d, e) exhibit positive SW feedbacks in the eastern Pacific, particularly for FGOALS-c4, where positive values can extend to the date line. To identify SW feedback biases, Li et al. (2014) proposed a decomposition method based on Lloyd et al. (2012), and decomposed the SW feedback into a total cloud-fraction feedback ( $\alpha_{\text{cltot}}$ ) a total liquid water path feedback ( $\alpha_{\text{lwp}}$ ) and a dynamics (vertical velocity at 500 hPa) feedback ( $\alpha_{\text{w500}}$ ). The feedback strengths are calculated as the regression coefficients of the total cloud, total liquid water path, and the vertical velocity at 500 hPa against the SST anomalies in the Niño-3 region, respectively, and are listed in Table 2. For the GAMIL2-related models (CESM-g2 and FGOALS-g2), all three strong component feedbacks contribute to the reasonably negative  $\alpha_{\text{sw}}$ . For FGOALS-c4, the much weaker  $\alpha_{\text{w500}}$ ,  $\alpha_{\text{lwp}}$  and the negative  $\alpha_{\text{cltot}}$  contribute to the negative  $\alpha_{\text{sw}}$  (turning positive) in the tropical eastern Pacific, while in CESM, the three terms are comparable to those of FGOALS-g2. To further investigate the source of the weak  $\alpha_{\text{sw}}$  in CESM, the vertical distributions of the cloud-fraction feedback and the cloud liquid water (CLD-LIQ) feedback are presented in Fig. 6. For the GAMIL2-related models (Fig. 6a, b), the cloud-fraction feedback and the CLDLIQ feedback are generally positive below 700 hPa in the Niño-3 region, while CAM4-related models exhibit strong negative values for the two feedbacks in the same region. Hence, the weaker negative  $\alpha_{\text{sw}}$  in CESM may be primarily due to low-layer negative cloud-related feedbacks. Positive  $\alpha_{\text{sw}}$  values are enhanced by the non-effective supplement in the upper levels. The vertical distributions of the cloud-fraction feedback and the CLDLIQ feedback in CAM4-related models in this study are consistent with those of the weak  $\alpha_{\text{sw}}$  groups in CMIP5 models (Fig. 4 in Li et al. 2015a), indicating a common feature related to strong ENSO variability. Li et al. (2015a) further pointed out that  $\alpha_{\text{sw}}$  biases are primarily affected by moist processes in atmospheric models. The enhanced stratiform processes in the GAMIL2 model play a key role in reducing SW feedback biases by affecting the profiles of cloud fraction and LWP when compared with previous versions (GAMIL1; Li et al. 2014). Based on multiple CMIP5 coupled and uncoupled models, Li et al. (2015a) found that the underestimation of SW feedbacks results from both weak negative SW responses to El Niño, particularly in the coupled models, and strong positive SW responses to La Niña. Stratiform processes play a more important role in SW feedbacks during La Niña, while

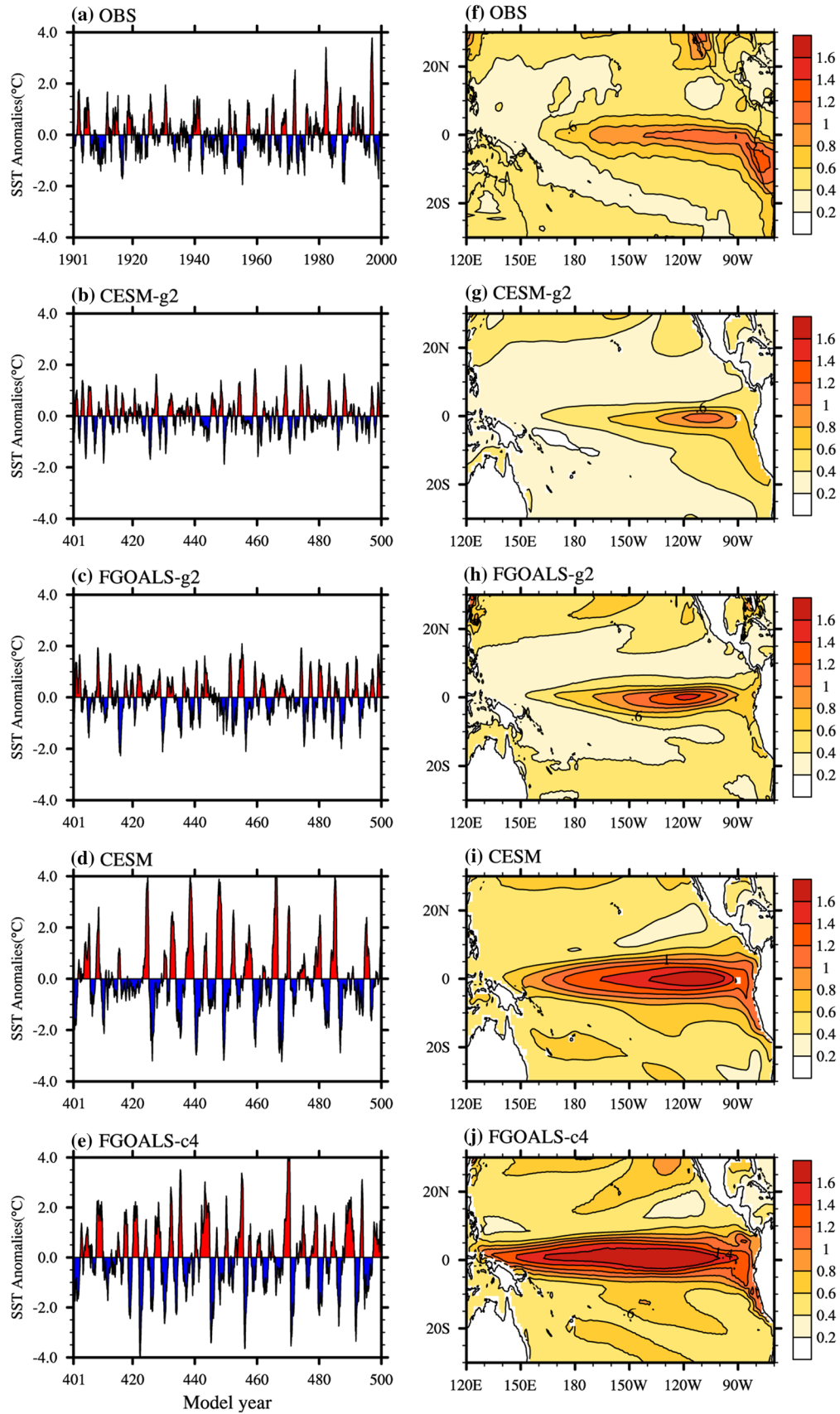


**Fig. 2** Time series of the Niño-3 index (a–e) and the spatial distributions of the SSTA standard deviations in the tropical Pacific (f–j) for HadISST observations during 1901–2000, and for CESM-g2, FGOALS-g2, CESM and FGOALS-c4 during the years 401–500 in the PI-control run

weakened convective processes, due to an excessive cold tongue, in the CMIP5 coupled models contribute more to the SW feedback biases during El Niño compared with the uncoupled models.

## 4.2 Differences in thermocline (TH) feedbacks

As shown in Fig. 3, the TH feedbacks of the GAMIL2-related models (CESM-g2 and FGOALS-g2) are underestimated by half, while those of the CAM4-related models (CESM and FGOALS-c4) are closer to the SODA-ERA40 data. It is worth noting that the difference in TH feedbacks between the FGOALS-g2 and CESM-g2 (CESM and FGOALS-c4) models with the same atmospheric component is only 18.1% (10.3%), while that between the CESM-g2 and CESM (FGOALS-g2 and FGOALS-c4) models with the same ocean component reaches 80.1% (92.9%), indicating that the atmospheric components (GAMIL2 and CAM4) not only dramatically affect the atmospheric feedback (TD) but also significantly affect the oceanic feedback (TH). As described in Sect. 2.2, the TH feedback is a product of four factors:  $\mu_a$  (response of the zonal wind stress anomaly to the SST anomaly),  $\beta_h$  (coefficient of regression of the zonal tilt of the thermocline and an equatorial zonal wind stress anomaly), the mean upwelling velocity  $\bar{w}$ , and  $a_h$  (coefficient of regression of the subsurface temperature anomalies on the thermocline depth averaged spatially in the eastern box). The underlying physical mechanism involves the SST anomaly occurring in the eastern Pacific, which induces a wind stress anomaly in the tropical Pacific basin, which then leads to an eastern–western thermocline depth anomaly, which in turn gives rise to a subsurface temperature anomaly in the eastern Pacific. Finally, the subsurface temperature anomaly together with the mean upwelling velocity strengthens the SST anomaly in the eastern tropical Pacific.

Values for the factors influencing the TH feedback discussed above are listed in Table 3 and are used to investigate the differences in TH feedbacks among the four parent models. Differences in TH feedbacks between the two atmospheric groups primarily come from  $\beta_h$ , whose value in the CAM4-related group is nearly 1.5 times greater than that in the GAMIL2-related group (the corresponding difference in the TH feedback is a factor of 2). It is also found that all four parent models underestimate the mean upwelling velocity to a certain extent, and the values of TH feedbacks for CESM and FGOALS-c4, which are closer to observations, are compensated by an overestimated  $\beta_h$ . This suggests

that an important factor in the observed TH feedback differences is  $\beta_h$ , which is calculated based on the Sverdrup balance and indicates how the zonal tilt of the thermocline anomaly responds to equatorial zonal wind stress anomaly forcing on an inter-annual timescale (Jin 1997; Philander 1981). Figure 7 shows scatter plots of the zonal tilt of the equatorial thermocline depth as a function of wind change with a regression fitting line for the four models. Blue labels indicate the regression coefficients for the individual models, which indicate that the atmospheric component can not only influence the regression coefficient ( $\beta_h$ ), but also affect the overall shape of the scatter plots. Data points for the GAMIL2-related group are short and confined, and those of the CAM4-related group are long and relatively dispersed.

Next, we explore the cause of the difference in  $\beta_h$  among the four models. Previous studies have suggested that the zonal wind stress in the tropical Pacific may excite eastward propagating Kelvin waves and westward propagating Rossby waves, leading to a west–east thermocline depth contrast pattern (Xiang et al. 2012). Figure 8 presents plots of the spatial patterns of the zonal wind stress anomaly regressed onto the equatorial zonal wind anomaly, averaged over the basin region (120°E–280°W, 5°S–5°N). Regression patterns among the four models show great differences between the two groups—i.e., the normalized wind stress anomaly over the Niño-4 region from the CAM4-related group (c and d) are larger than those of the GAMIL2-related group (a and b). This suggests that the CAM4-related group obtains stronger thermocline–wind coupling, which leads to a stronger  $\beta_h$ , because equatorial zonal wind in the Niño-4 region is more relevant than other regions to ENSO events.

In addition, the ocean subsurface cold bias, particularly in the central equatorial Pacific, could affect the thermocline slope response sensitivity to wind change (Kim et al. 2017). Figure 9 shows a vertical cross-section of the biases of the climatological mean ocean temperatures (contours) and the vertical gradients (shading) along the equator in the four parent coupled models compared with the SODA reanalysis. It is worth noting that the apparent cold biases in all four simulations are mainly due to the different periods between the simulations (during the pre-industrial period) and the reanalysis data (for the years 1950–1999). The GAMIL2-based models (Fig. 9a, b) exhibit noticeably colder ocean subsurface temperature biases than do the CAM4-based models (Fig. 9c, d) in the central equatorial Pacific, particularly near the thermocline depth (black dotted line in Fig. 9). Corresponding to the enhanced cold biases, the GAMIL2-based models simulate much larger vertical ocean temperature gradients than do the CAM4-related models above the equatorial thermocline (shading in Fig. 9), particularly near the thermocline depth. As the increasing thermal stratification in the upper ocean may confine wind-forced momentum (Kim et al. 2017), the smaller vertical temperature gradients

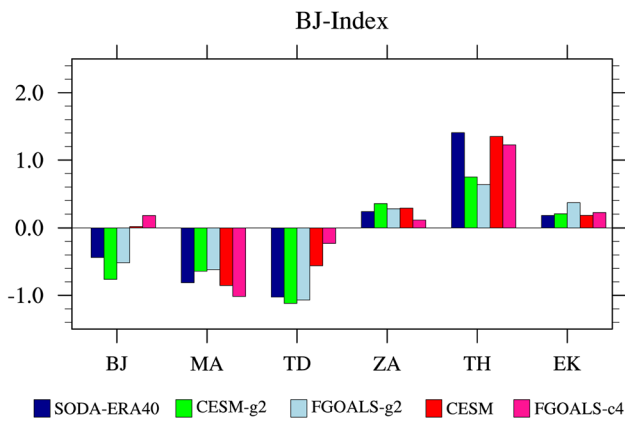


**Fig. 3** Bjerknes stability index (BJ-index) and corresponding contributing terms for the reanalysis products of SODA-ERA40 (dark blue bars), CESM-g2 (green bars), FGOALS-g2 (light blue bars), CESM (red bars) and FGOALS-c4 (pink bars)

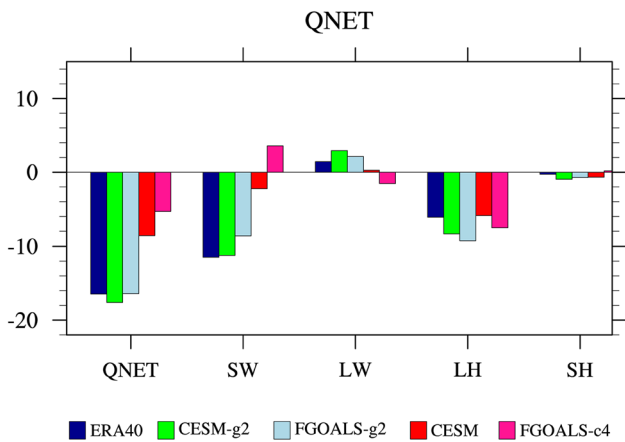


**Fig. 4** Net heat-flux feedback and corresponding contributing terms for the ERA40 (dark blue bars), CESM-g2 (green bars), FGOALS-g2 (light blue bars), CESM (red bars) and FGOALS-c4 (pink bars)

in the CAM4-based models lead to a stronger response of the thermocline to the surface wind than is the case for the GAMIL2-based models.

It should be noted that both the differences of the normalized wind stress anomaly over the Niño-4 region and of the vertical ocean subsurface temperature cold biases contribute to the differing  $\beta_h$  among the four simulations, and both differences result from the atmospheric component. In addition to the above factors, the meridional shape of the zonal wind stress response to the eastern equatorial Pacific SST change and the mean thermocline depth may have influenced the

thermocline feedback and the sensitivity of the zonal thermocline in previous studies (Chen et al. 2015a, b, 2016; Im et al. 2015). However, the mean thermocline depth (Fig. 9) and the wind stress pattern (not shown) in this study do not noticeably differ among the four simulations, and are thus unlikely to lead to the differences of thermocline feedback shown in Table 3.

## 5 Summary and discussion

### 5.1 Summary

In order to investigate to what extent the atmospheric and the oceanic model components of coupled models affect ENSO amplitude simulations, we assemble four coupled models and carry out analyses on their ENSO simulations. Specifically, the atmospheric and oceanic components of two commonly used coupled models with very different ENSO characteristics are cross-coupled to construct four parent models: CESM-g2, FGOALS-g2, CESM and FGOALS-c4. Simulated ENSO behaviours from individual PI-control experiments (year 401–500) using the four models are compared by performing a BJ-index analysis. The main conclusions are summarized in the following paragraphs.

By comparing the simulated ENSO amplitude with that of observations, the four models are separated into two groups: the CESM and FGOALS-c4, which share the same atmospheric component (CAM4), fall into the ‘strong ENSO amplitude’ group, and the CESM-g2 and FGOALS-g2, which share the same atmospheric component (GAMIL2), fall into the ‘weak ENSO amplitude’ group. It should be noted that the ENSO amplitude from FGOALS-g2 is close to observations, despite the presence of FGOALS-g2 in the second group. The ENSO amplitude in the first group reaches twice that of the second group, while the differences within each group are relatively small, indicating the dominant role of the atmospheric model in ENSO amplitude simulations.

The BJ-index is employed to investigate how the atmospheric and oceanic components of the four parent models affect ENSO simulations. It is found that the main sources of the ENSO amplitude differences between the two groups are the thermodynamic (TD) feedback and the thermocline (TH) feedback. The GAMIL2-related group reproduces a relatively realistic TD term compared to reanalysis data (SODA-ERA40), while the CAM4-related group underestimates the damping effect of the TD feedback by more than half. This underestimation arises from the shortwave



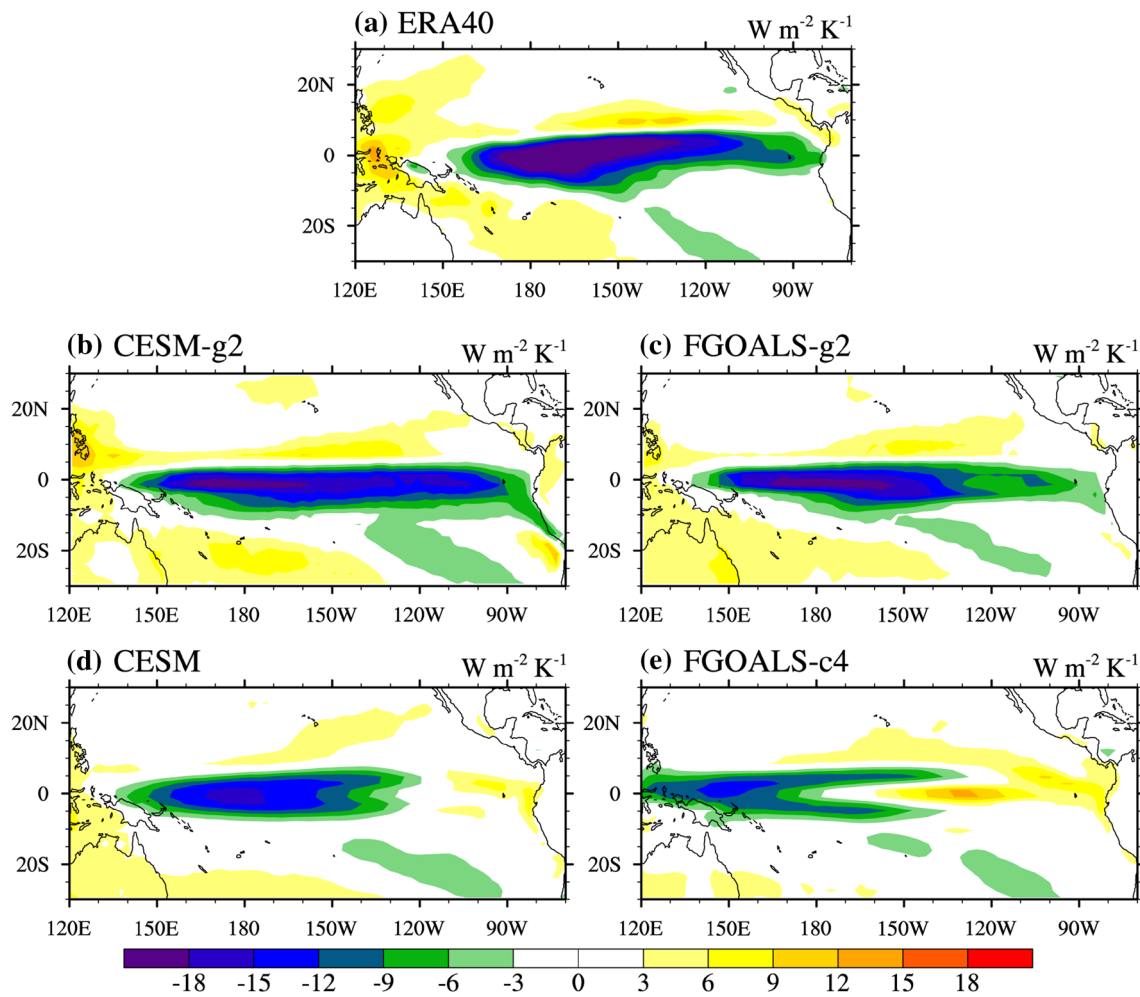


**Fig. 5** Shortwave flux feedbacks in the tropical Pacific for (a) ERA40, (b) CESM-g2, (c) FGOALS-g2, (d) CESM and (e) FGOALS-c4, calculated by a linear regression of the SW anomaly against the Niño-3 SST anomaly ( $W m^{-2} K^{-1}$ )

**Table 2** Coefficients of linear regression against SST of: surface shortwave radiation ( $W m^{-2} K^{-1}$ ), 500-hPa vertical velocity ( $hPa day^{-1} K^{-1}$ ), total-, high-, middle-, and low-cloud fraction ( $\% K^{-1}$ ), and total liquid water path ( $g m^{-2} K^{-1}$ ) over the Niño-3 region from observations, CESM-g2, FGOALS-g2, CESM and FGOALS-c4

	OBS	CESM-g2	FGOALS-g2	CESM	FGOALS-c4
$\alpha_{sw}$	- 11.49 (ERA40)	- 11.24	- 8.57	- 2.25	3.58
$\alpha_{w500}$	- 11.32/- 5.63 (ERA40/Oaflux)	- 11.56	- 8.83	- 8.08	- 3.23
$\alpha_{lwp}$	19.9/4.42 (ISCCP)	13.13	9.83	10.49	0.52
$\alpha_{cldtot}$	4.52 (ISCCP)	4.84	3.47	3.02	- 0.86
$\alpha_{cldhgh}$	3.45 (ISCCP)	4.44	3.98	8.79	5.86
$\alpha_{cldmid}$	2.76 (ISCCP)	3.66	2.73	4.67	2.25
$\alpha_{cldlow}$	-0.42 (ISCCP)	3.90	2.26	- 3.46	- 4.75

(SW) feedback. As indicated by a comparison of results from the GAMIL2-related group and observations, the weaker SW feedback in the CAM-related group is attributable to a negative low-cloud fraction feedback, a negative

low-cloud liquid water feedback, and a dynamics feedback in the Niño-3 region. The GAMIL2-related group underestimates the positive TH term by nearly half, while the CAM4-related group reproduces a more accurate value. A

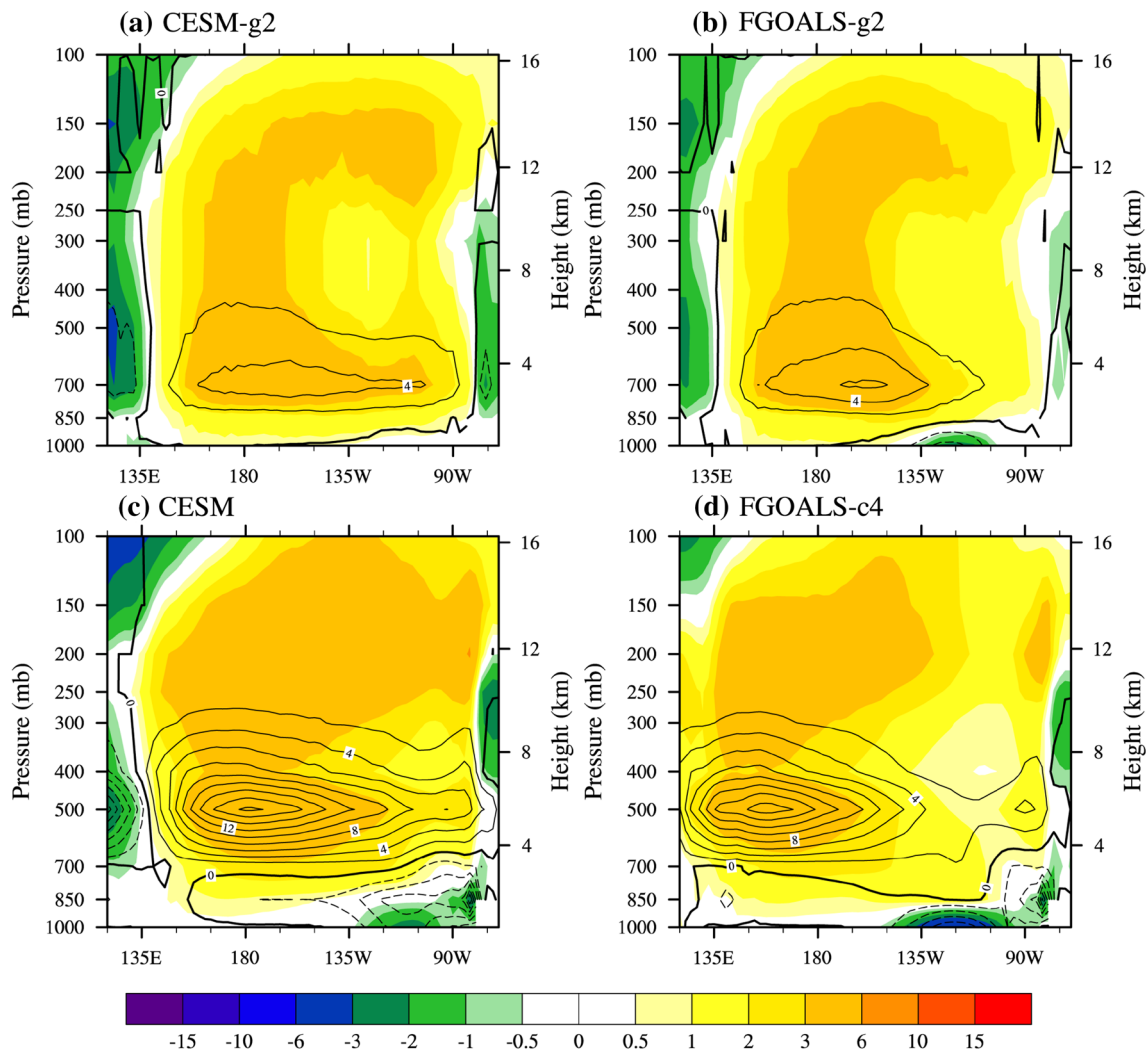


**Fig. 6** Vertical distribution of the cloud-fraction feedback (shaded) and cloud liquid amount (CLDLIQ) feedback (contours) for **a** CESM-g2, **b** FGOALS-g2, **c** CESM and **d** FGOALS-c4, averaged over the

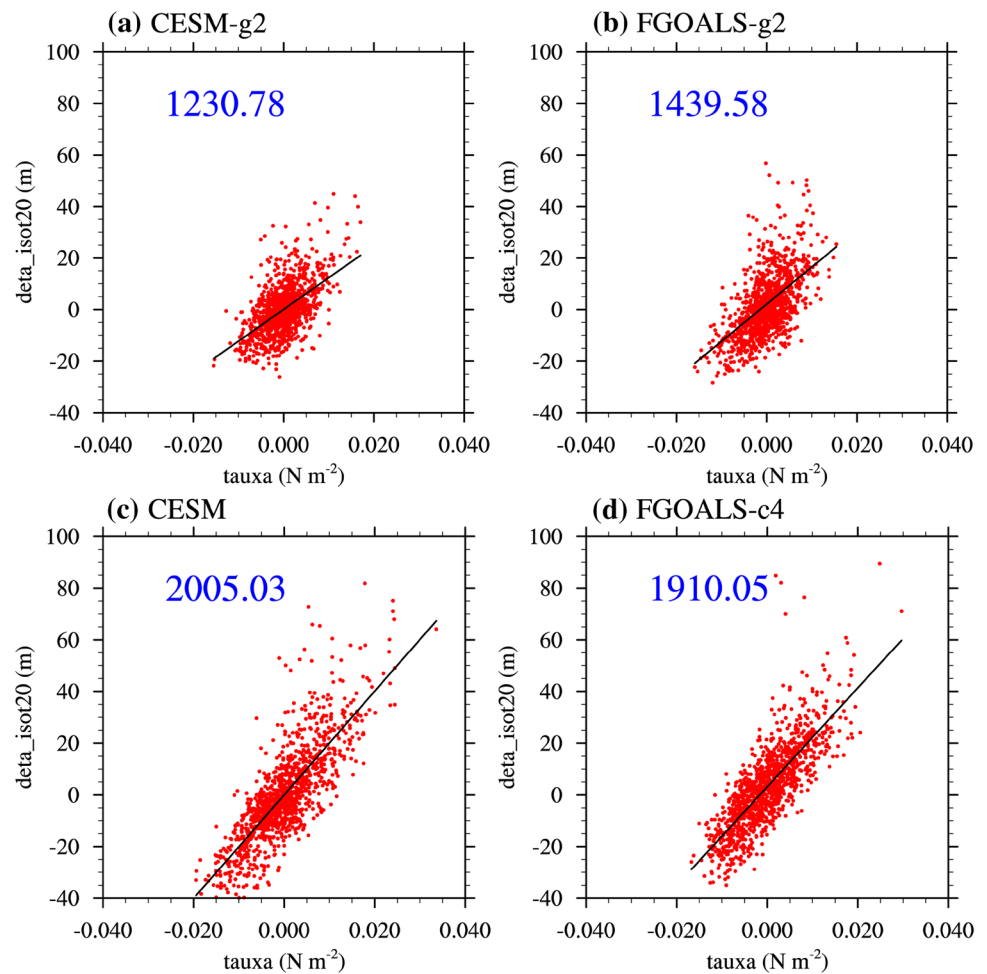
equatorial Pacific (5°N–5°S; units: percent for cloud fraction and  $10^{-6} \text{ kg kg}^{-1}$  for CLDLIQ)

**Table 3** Thermocline (TH) feedbacks and their four components from the reanalysis products of SODA-ERA40 and the four parent models (CESM-g2, FGOALS-g2, CESM and FGOALS-c4)

	SODA-ERA40	CESM-g2	FGOALS-g2	CESM	FGOALS-c4
TH	1.404	0.749	0.634	1.349	1.223
$\mu_a$	0.00401	0.00412	0.00363	0.00423	0.00367
$\beta_h$	1513.26	1230.78	1439.58	2005.03	1910.05
$a_h$	0.121	0.134	0.101	0.121	0.143
$\langle \frac{\bar{w}}{H_1} \rangle_E$	$1.2e-07$	$7.0e-08$	$7.6e-08$	$8.4e-08$	$7.8e-08$

$\mu_a$  is measured as the response of the zonal wind stress anomaly to the SST anomaly;  $\beta_h$  is the coefficient of regression of the zonal tilt of the thermocline and the equatorial zonal wind stress anomaly;  $a_h$  is the coefficient of regression of the subsurface temperature anomalies on the thermocline depth, averaged spatially in the eastern box;  $\bar{w}$  denotes the mean upwelling velocity

**Fig. 7** Scatterplots of the zonal tilt of the equatorial thermocline depth as a function of wind change (red dots) for the four parent models; the slope of the black fitting lines indicate  $\beta_h$ , whose values are shown in blue [Units:  $\text{m}/(\text{N m}^{-2})$ ]



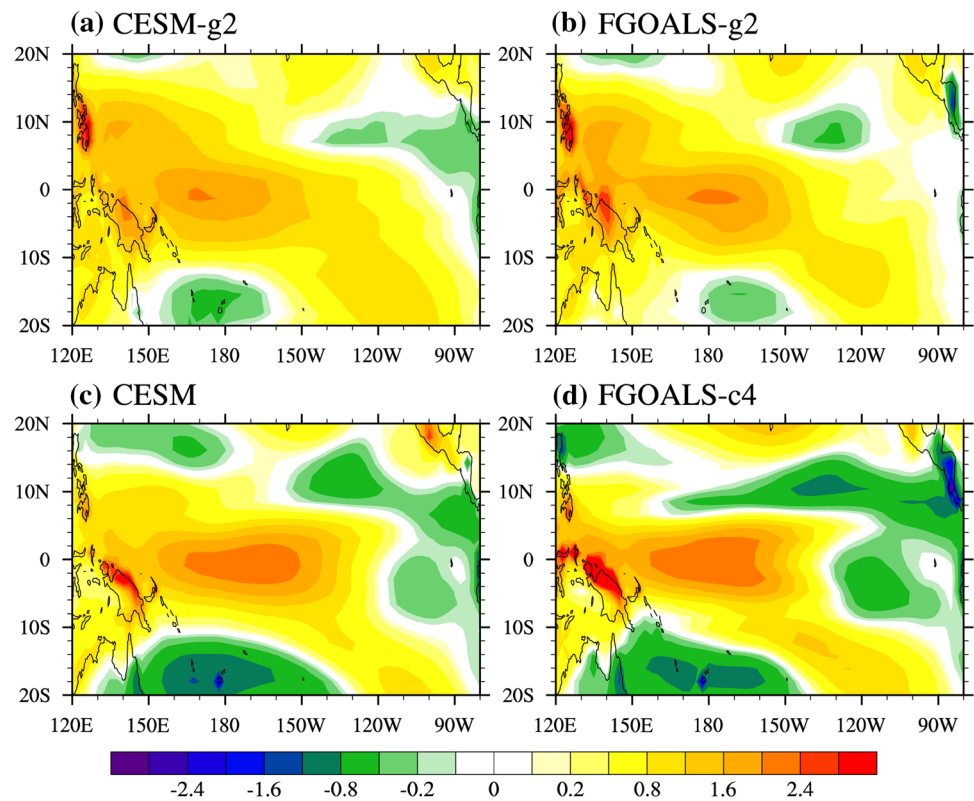
regression of zonal tilt of the thermocline on the equatorial zonal wind stress ( $\beta_h$ ) is correlated with TH feedback differences between the two groups, which are closely associated with the normalized wind stress anomaly over the Niño-4 region and the vertical ocean subsurface temperature cold biases among the four simulations, and both differences result from the atmospheric component. In addition, the realistic simulated value for TH is, to some extent, due to compensation by the overestimated  $\beta_h$  and the underestimated  $\bar{w}$  in the CAM4 group.

This study indicates that the atmospheric component of coupled models plays a dominant role in ENSO amplitude through both the atmospheric thermodynamic feedback and the oceanic thermocline feedback.

## 5.2 Discussion

In this study, differences in the atmospheric TD feedback and the oceanic TH feedback are both traced to the atmospheric component of four coupled models. In addition to moist processes, model resolution and different tuning options (Guilyardi et al. 2009; Li et al. 2015a; Toniazzo et al. 2008) in the two atmospheric components may contribute to TD feedback differences. The TD feedback biases may also be linked to mean state biases (Ferrett et al. 2018), and warrant further exploration. The normalized zonal wind stress anomaly is a key factor in TH feedback differences. Furthermore, the zonal wind stress may be associated with SST gradients (Lindzen and

**Fig. 8** Spatial patterns of the normalized zonal wind stress anomaly for the four parent models: **a** CESM-g2, **b** FGOALS-g2, **c** CESM and **d** FGOALS-c4. The normalized zonal wind stress anomaly is calculated as the zonal wind stress anomaly regressed onto the equatorial zonal wind anomaly averaged over the basin region (120°E–280°W, 5°S–5°N)

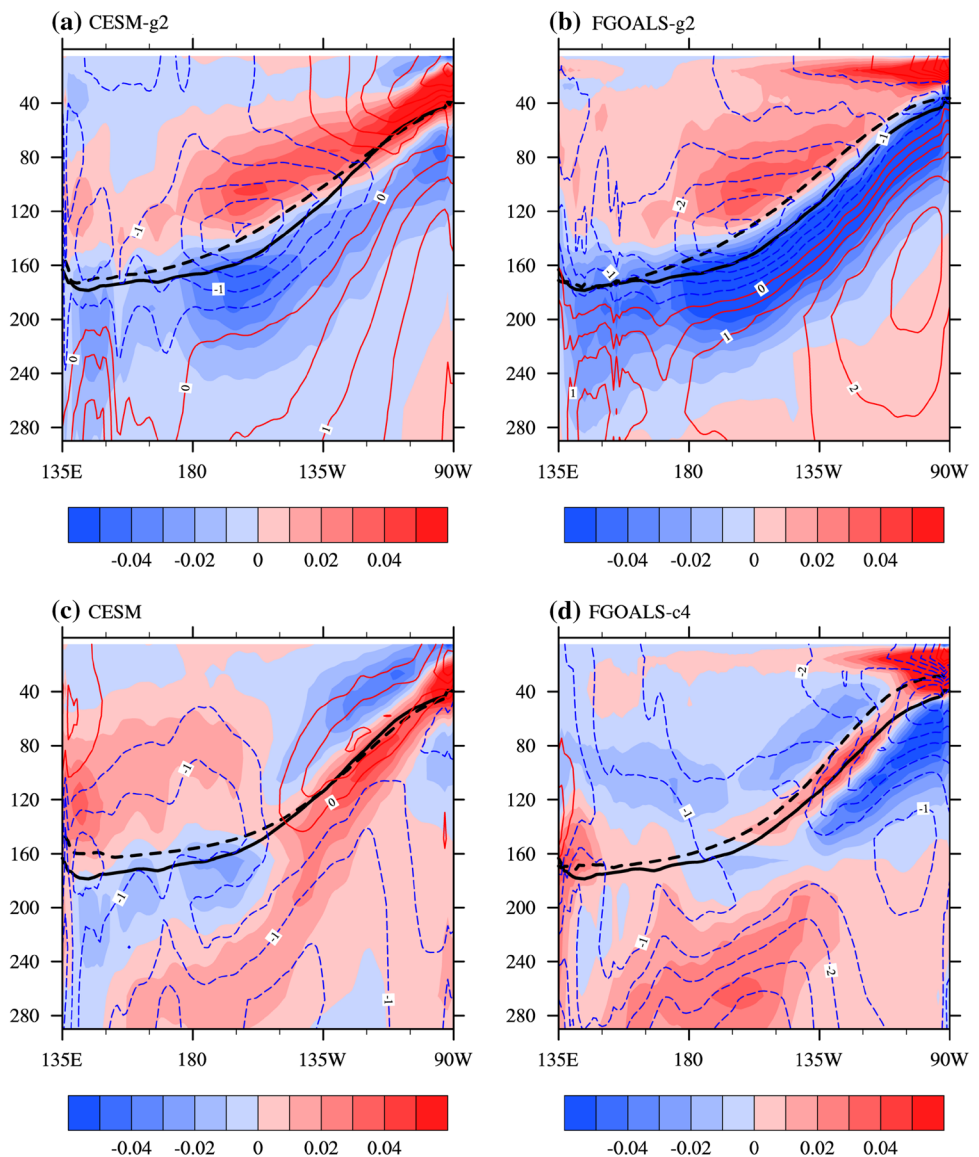


Nigam 1987) and the diabatic heating (DH; Gill 1980). The DH contributions may stem from the free atmosphere or physical processes, such as moist processes, radiation, and vertical diffusion (Li et al. 2015b; Xie et al. 2017). The impact of the choice of atmospheric component on TH differences may be affected by SST gradients or DH, and should be the subject of future analysis. Other key factors for TH feedback differences are the cold climatological ocean subsurface temperature biases caused by the atmospheric component. As for the manner in which the atmospheric component affects the oceanic temperature biases, wind velocity at 10 meters (U10 and V10) have been regarded as the most important variable to be corrected in order to obtain reasonable surface ocean conditions in the Mediterranean Sea, while air temperature and cloud cover had a more marginal importance in reducing the SST bias (Macias et al. 2018); Moreover, errors in the location of the maximum wind stress in the Southern Hemisphere were also thought to contribute to the temperature biases of the Southern Ocean via their influence on the water masses (Gupta et al. 2009; Russell

et al. 2006); In addition, by performing sensitivity experiments in an ocean-ice model and nudging experiments in the FGOALS-g2 model, Shi et al. (2018) found that the warm bias in SST over the Atlantic Cold Tongue region can be attributed to the biases of westerly wind along the equator, northerly wind over the southern tropical Atlantic, surface specific humidity, surface air temperature, and downward shortwave radiation, and the former two terms play the most important role. It warrants future investigation that how do the above or other factors of atmospheric component affect the ocean vertical temperature and its stratification in this study.

Among the terms that contribute to the BJ-index, differences in the damping mean advection (MA) feedbacks between the two atmospheric groups are not negligible, despite not greatly affecting the TD and TH terms. The MA term may be linked to the ocean temperature and velocity distribution around the boundary of the BJ-index box through the mixed layer, and the mechanism of such a linkage should be explored in future research.

**Fig. 9** Vertical cross-section of the biases of the climatological ocean temperatures (contours; contour interval = 0.5 °C) and the vertical gradients (shading) along the equator (2°S–2°N) in the four parent coupled models during years 401–500 in the PI-control run compared with the SODA reanalysis during the years 1950–1999. The thermocline depth from four simulations (black dashed lines) and the reanalysis (black solid lines) are also shown



It is also worth noting that the BJ index proposed by Jin (1996) is based on a linear approximation, it may not capture the effects of nonlinearity, noise and seasonal cycles (Fedorov 2002; An 2008; Zavala-Garay et al. 2003), which may also influence ENSO variability. Whether such factors should be considered under certain conditions (such as during strong El Niño events) should be further evaluated. In addition, although this paper demonstrates the dominant role of the atmospheric component of coupled models, other processes related to the oceanic component may also have important influences on simulated ENSO amplitude.

**Acknowledgements** This work was funded by the National Natural Science Foundation of China (grant nos. 41622503; 41605061), the China Postdoctoral Science Foundation (grant no. 1191005829),

the National Key Research Project (grant no. 2016YFB0200805), and the National Key Basic Research Program of China (grant no. 2015CB954101).

## References

- An SI (2008) Interannual variations of the tropical ocean instability wave and ENSO. *J Clim* 21:3680–3686
- An SI, Choi J (2013) Inverse relationship between the equatorial eastern Pacific annual cycle and ENSO amplitudes in a coupled general circulation model. *Clim Dyn* 40:663–675
- An SI, Jin FF (2001) Collective Role of Thermocline and Zonal Advective Feedbacks in the ENSO Mode. *J Clim* 14:3421–3432

- An SI, Heo ES, Kim ST (2017) Feedback process responsible for intermodel diversity of ENSO variability. *Geophys Res Lett* 44:4272–4279
- Bellenger H, Guilyardi E, Leloup J, Lengaigne M, Vialard J (2014) ENSO representation in climate models: from CMIP3 to CMIP5. *Clim Dyn* 42:1999–2018
- Callaghan J, Power SB (2011) Variability and decline in the number of severe tropical cyclones making land-fall over eastern Australia since the late nineteenth century. *Clim Dyn* 37:647–662
- Carton JA, Giese BS (2008) A reanalysis of ocean climate using simple ocean data assimilation. *Mon Weather Rev* 136:2999–3017
- Chen L, Yu Y, Sun DZ (2013) Cloud and water vapor feedbacks to the El Niño warming: are they still biased in CMIP5 models? *J Clim* 26:4947–4961
- Chen D et al (2015a) Strong influence of westerly wind bursts on El Niño diversity. *Nature Geosci* 8:339–345
- Chen L, Li T, Yu Y (2015b) Causes of strengthening and weakening of ENSO amplitude under global warming in four CMIP5 models. *J Clim* 28:3250–3274
- Chen L, Yu Y, Zheng W (2016) Improved ENSO simulation from climate system model FGOALS-g1.0 to FGOALS-g2. *Clim Dyn* 47:2617–2634
- Chen L, Li T, Yu Y, Behera SK (2017) A possible explanation for the divergent projection of ENSO amplitude change under global warming. *Clim Dyn* 49:3799–3811. <https://doi.org/10.1007/s00382-017-3544-x>
- Christensen JH et al (2013) Climate phenomena and their relevance for future regional climate change. In: *Climate change 2013: the physical science basis. Contribution of Working Group I to the Fifth Assessment Report of the Intergovernmental Panel on Climate Change*. Cambridge University Press, Cambridge
- Dommengat D (2010) The slab ocean El Niño. *Geophys Res Lett* 37:L20701. <https://doi.org/10.1029/2010GL044888>
- Donnelly JP, Woodruff JD (2007) Intense hurricane activity over the past 5000 years controlled by El Niño and the west African monsoon. *Nature* 447:465–468
- Fedorov AV (2002) The response of the coupled tropical atmosphere to westerly wind bursts. *Q J R Meteorol Soc* 128:1–23
- Ferrett S, Collins M, Ren HL (2018) Diagnosing relationships between mean state biases and El Niño shortwave feedback in CMIP5 models. *J Clim* 31:1315–1335
- Giese BS, Ray S (2011) El Niño variability in simple ocean data assimilation (SODA), 1871–2008. *J Geophys Res* 116:C02024. <https://doi.org/10.1029/2010JC006695>
- Gill AE (1980) Some simple solutions for heat-induced tropical motion. *Q J R Meteorol Soc* 106:447–462
- Guilyardi E (2006) El Niño–mean state–seasonal cycle interactions in a multi-model ensemble. *Clim Dyn* 26:329–348
- Guilyardi E, Gualdi S, Slingo J et al (2004) Representing El Niño in coupled ocean–atmosphere GCMs: The dominant role of the atmosphere component. *J Clim* 17:4623–4629
- Guilyardi E, Braconnot P, Jin FF, Kim ST, Kolasinski M, Li T, Musat I (2009) Atmosphere feedbacks during ENSO in a coupled GCM with a modified atmospheric convection scheme. *J Clim* 22:5698–5718
- Guilyardi E, Bellenger H, Collins M, Ferrett S, Cai W, Wittenberg A (2012) A first look at ENSO in CMIP5. *CLIVAR Exch* 58:29–32
- Gupta AS, Santoso A, Taschetto AS, Ummenhofer CC, Trevena J, England MH (2009) Projected changes to the southern hemisphere ocean and sea ice in the IPCC AR4 climate models. *J Clim* 22:3047–3078
- Hammer GL, Hansen JW, Phillips JG et al (2001) Advances in the application of climate prediction in agriculture. *Agric Syst* 70:515–553
- Hunke EC, Lipscomb WH (2008) CICE: the los alamos sea ice model user's manual, Version 4. Los Alamos National Laboratory Tech. Rep. LA-CC-06-012, 76 pp
- Hurrell JW, Hack JJ, Shea D, Caron JM, Rosinski J (2008) A new sea surface temperature and sea ice boundary dataset for the community atmosphere model. *J Clim* 21:5145–5153
- Im SH, An SI, Kim ST, Jin FF (2015) Feedback processes responsible for El Niño–La Niña amplitude asymmetry. *Geophys Res Lett* 42:5556–5563
- Jin F-F (1996) Tropical ocean–atmosphere interaction, the Pacific cold tongue, and the El Niño–Southern oscillation. *Science* 274:76–78
- Jin F-F (1997) An equatorial ocean recharge paradigm for ENSO. Part II: A stripped-down coupled model. *J Atmos Sci* 54:830–847
- Jin F-F, Kim ST, Bejarano L (2006) A coupled stability index for ENSO. *Geophys Res Lett* 33:L23708. <https://doi.org/10.1029/2006GL027221>
- Kim ST, Jin F-F (2010) An ENSO stability analysis. Part II: results from the twentieth and twenty-first century simulations of the CMIP3 models. *Clim Dyn* 36(7):1609–1627
- Kim ST, Jin F-F (2011a) An ENSO stability analysis. Part I: results from a hybrid coupled model. *Clim Dyn* 36:1593–1607
- Kim ST, Jin F-F (2011b) An ENSO stability analysis. Part II: results from the twentieth and twenty-first century simulations of the CMIP3 models. *Clim Dyn* 36:1609–1627
- Kim ST, Cai W, Jin F-F, Santoso A, Wu L, Guilyardi E, An S-I (2014) Response of El Niño sea surface temperature variability to greenhouse warming. *Nat Clim Change* 4:786–790
- Kim ST, Jeong H-I, Jin F-F (2017) Mean bias in seasonal forecast model and ENSO prediction error. *Sci Rep* 7(1):6029
- Kovats RS, Bouma MJ, Hajat S, Worrall E, Haines A (2003) El Niño and health. *Nature* 361:1481–1489
- Li LJ, Lin PF, Yu YQ et al (2013a) The flexible global ocean–atmosphere–land system model, grid-point Version 2: FGOALS-g2. *Adv Atmos Sci* 30:543–560
- Li LJ, Wang B, Dong L, Liu L, Shen S, Hu N, Sun WQ, Wang Y, Huang WY, Shi XJ, Pu Y, Yang GW (2013b) Evaluation of grid-point atmospheric model of IAP LASG Version 2 (GAMIL2). *Adv Atmos Sci* 30:855–867
- Li LJ, Wang B, Zhang GJ (2014) The role of nonconvective condensation processes in response of surface shortwave cloud radiative forcing to El Niño warming. *J Clim* 27:6721–6735
- Li LJ, Wang B, Zhang GJ (2015a) The role of moist processes in shortwave radiative feedback during ENSO in the CMIP5 Models. *J Clim* 28:9892–9908
- Li LJ, Wang B, Zhou TJ (2015b) Direct effect of lower-tropospheric diabatic heating on surface winds over the equatorial Pacific in three atmospheric general circulation model simulations. *Atmos Sci Lett* 16:96–102
- Liu HL, Lin PF, Yu YQ, Zhang XH (2012) The baseline evaluation of LASG/IAP climate system ocean model (LICOM) version 2.0. *Acta Meteorologica Sinica* 26:318–329
- Lloyd J, Guilyardi E, Weller H (2012) The role of atmospheric feedbacks during ENSO in CMIP3 models. Part III: the shortwave flux feedback. *J Clim* 25:4275–4293
- Lübbecke JF, McPhaden MJ (2013) A comparative stability analysis of Atlantic and Pacific Niño modes. *J Clim* 26:5965–5980
- Macias D, Garcia-Gorriç E, Dosio A, Stips A, Keuler K (2018) Obtaining the correct sea surface temperature: bias correction of regional climate model data for the Mediterranean Sea. *Clim Dyn* 51:1095–1117
- McPhaden MJ, Zebiak SE, Glantz MH (2006) ENSO as an integrating concept in earth science. *Science* 314:1740–1745
- Meehl GA, Gent PR, Arblaster JM, Otto-Bliniesner BL, Brady EC, Craig A (2001) Factors that affect the amplitude of El Niño in global coupled climate models. *Clim Dyn* 17:515–526

- Neale RB, Richter JH, Jochum M (2008) The impact of convection on ENSO: from a delayed oscillator to a series of events. *J Clim* 21:5904–5924
- Neale RB, Richter J, Park S, Lauritzen PH, Vavrus SJ, Rasch PJ, Zhang M (2013) The mean climate of the community atmosphere model (CAM4) in forced SST and fully coupled experiments. *J Clim* 26:5150–5168
- Oleson KW et al (2010) Technical description of version 4.0 of the Community Land Model (CLM). NCAR Tech. Note NCAR/TN-478 + STR, 257 pp
- Philander SGH (1981) The response of equatorial oceans to a relaxation of the trade winds. *J Phys Oceanogr* 11:176–189
- Rädel G, Mauritsen T, Stevens B, Dommenget D, Matei D, Bellomo K, Clement A (2016) Amplification of El Niño by cloud longwave coupling to atmospheric circulation. *Nat Geosci* 9:106–110
- Rossow WB, Schiffer RA (1999) Advances in understanding clouds from ISCCP. *B Am Met Soc* 80:2261–2288
- Russell JL, Stouffer RJ, Dixon KW (2006) Intercomparison of the southern ocean circulations in IPCC coupled model control simulations. *J Clim* 19:4560–4575
- Shi Y, Huang W, Wang B, Yang Z, He X, Qiu T (2018) Origin of warm SST bias over the Atlantic Cold tongue in the coupled climate model FGOALS-g2. *Atmosphere* 9:275. <https://doi.org/10.3390/atmos9070275>
- Smith RD, Jones P, Briegleb B et al (2010) The parallel ocean program (POP) reference manual. Los Alamos National Laboratory Tech. Rep. LAUR-10-01853, 140 pp
- Stevenson SL (2012) Significant changes to ENSO strength and impacts in the twenty-first century: results from CMIP5. *Geophys Res Lett* 39:L17703. <https://doi.org/10.1029/2012GL052759>
- Sun DZ, Zhang T, Covey C et al (2006) Radiative and dynamical feedbacks over the equatorial cold tongue: results from nine atmospheric GCMs. *J Clim* 19:4059–4074
- Sun DZ, Yu Y, Zhang T (2009) Tropical water vapor and cloud feedbacks in climate models: a further assessment using coupled simulations. *J Clim* 22:1287–1304
- Tang YL, Li LJ, Dong WJ, Wang B (2016) Tracing the source of ENSO simulation differences to the atmospheric component of two CGCMs. *Atmos Sci Lett* 17:155–161
- Toniazzo T, Collins M, Brown J (2008) The variation of ENSO characteristics associated with atmospheric parameter perturbations in a coupled model. *Clim Dyn* 30:643–656
- Uppala SM, Kållberg PW, Simmons AJ et al (2005) The ERA-40 Re-Analysis. *Q J R Meteorol Soc* 131:2961–3012
- Wang B, Wan H, Ji ZZ, Zhang X, Yu RC, Yu YQ, Liu HT (2004) Design of a new dynamical core for global atmospheric models based on some efficient numerical methods. *Sci China Math* 47:4–21
- Wu F, Liu H, Li W, Zhang X (2005) Effect of adjusting vertical resolution on the eastern equatorial Pacific cold tongue. *Acta Meteorologica Sinica* 24:1–12
- Xiang B, Wang B, Ding Q et al (2012) Reduction of the thermocline feedback associated with mean SST bias in ENSO simulation. *Clim Dyn* 39:1413–1430
- Xie F, Xue W, Li LJ, Zhang T, Wang B, Xu S (2017) Quantification of the responses of equatorial Pacific surface wind to uncertain cloud-related parameters in GAMIL2. *Atmos Sci Lett* 18:458–465
- Yu JY, Kim ST (2010) Identification of central-Pacific and eastern-Pacific types of ENSO in CMIP3 models. *Geophys Res Lett* 37:L15705. <https://doi.org/10.1029/2010GL044082>
- Zavala-Garay J, Moore AM, Perez CL, Kleeman R (2003) The response of a coupled model of ENSO to observed estimates of stochastic forcing. *J Clim* 16:2827–2842